LASER & PHOTONICS REVIEWS
www.lpr-journal.org

Metasurface Enabled Multi-Target and Multi-Wavelength Diffraction Neural Networks

Haoxiang Chi, Xiaofei Zang, Teng Zhang, Guannan Wang, Zhiyuan Fan, Yiming Zhu,* Xianzhong Chen,* and Songlin Zhuang*

Benefiting from low power consumption and high processing speed, there is a growing interest in diffraction neural networks (DNNs), which are typically showcased with 3D printing devices, leading to large volumes, high costs, and low levels of integration. Metasurfaces can desirably manipulate wavefronts of electromagnetic waves, providing a compact platform for mimicking DNNs with novel functions. Although multi-wavelength and multi-target recognition provides a richer and more detailed understanding of complex environments, existing architectures are primarily trained to classify a single target at a specific wavelength. A metasurface approach is proposed to design multiplexed DNNs that can classify multiple targets and spatial sequences across various wavelengths in multiple channels. To realize multi-task processing, the dielectric metasurface is designed based on phase and wavelength multiplexing, which can integrate multi-target DNNs with different tasks such as operating at distinct wavelengths and classifying diverse targets. The efficacy of this method is exemplified through the numerical simulation and experimental demonstration of recognizing a single target with two wavelengths, two targets at a single wavelength, and two targets at dual wavelengths. This compact metasurface approach enables the design of multi-target and multi-wavelength DNNs, opening a new window to develop massively parallel processing and versatile artificial intelligence systems.

1. Introduction

Deep learning, a kind of artificial neural network (ANN) model, draws inspiration from the structures of human brains, enabling training for analyzing and processing input data with unprecedented capabilities in image processing and pattern recognition.[1–5] Its uniqueness in continuous training and learning has led to applications in various fields, including object detection, image classification, speech recognition, and language translation.[6–10] However, the deep learning is a data-driven algorithm and the realization of its versatile functions (or parallel computing) in deep learning-based architecture comes at the cost of computing resources and large-scale datasets. The frequent reading and writing of huge volumes of data on existing electronic computers inevitably leads to significant energy consumption. Furthermore, the mismatch between data reading and processing speed can degrade computing performance, which is another bottleneck of ANN.

Optical neural networks (ONNs) have garnered significant attention recently due to their advantages in parallel processing, lower energy consumption, and high-speed characteristics.[11–15] As one type of ONNs, all-optical diffraction deep neural networks (D^2NNs) have been proposed and demonstrated for image recognition and handwritten digit classification.[16,17] In addition to these applications, D^2NNs have also been used to realize various functions such as optical logic operations, pulse shaping, information encryption, and OAM beam multiplexing/demultiplexing.[18–22] These unique functions rely on constructing 3D printing diffractive surfaces, which suffer from large volume, high cost, and low level of integration. Metasurfaces, 2D counterparts of metamaterials, have shown remarkable capabilities in manipulating the wavefront of electromagnetic (EM) waves, leading to novel applications, including beam steering,[23–25] polarization conversion,[26–28] vortex generation,[29–31] metalenses,[32–37] and holograms.[38–43] Unlike traditional 3D printing devices that rely on phase accumulation during propagation, metasurfaces can generate abrupt phase changes at planar meta-atom interfaces, providing a flexible

H. Chi, X. Zang, T. Zhang, G. Wang, Z. Fan, Y. Zhu, S. Zhuang
Terahertz Technology Innovation Research Institute, Terahertz Spectrum and Imaging Technology Cooperative Innovation Center, Shanghai Key Lab of Modern Optical System
University of shanghai for Science and Technology
Shanghai, China
E-mail: xfzang@usst.edu.cn; ymzhu@usst.edu.cn

X. Chen
SUPA, Institute of Photonics and Quantum Sciences, School of Engineering and Physical Sciences
Heriot-Watt University
EH14 4AS Edinburgh, United Kingdom
E-mail: x.chen@hw.ac.uk

X. Zang, Y. Zhu
Shanghai Institute of Intelligent Science and Technology
Tongji University
Shanghai, China

The ORCID identification number(s) for the author(s) of this article can be found under https://doi.org/10.1002/lpor.202401178

DOI: 10.1002/lpor.202401178

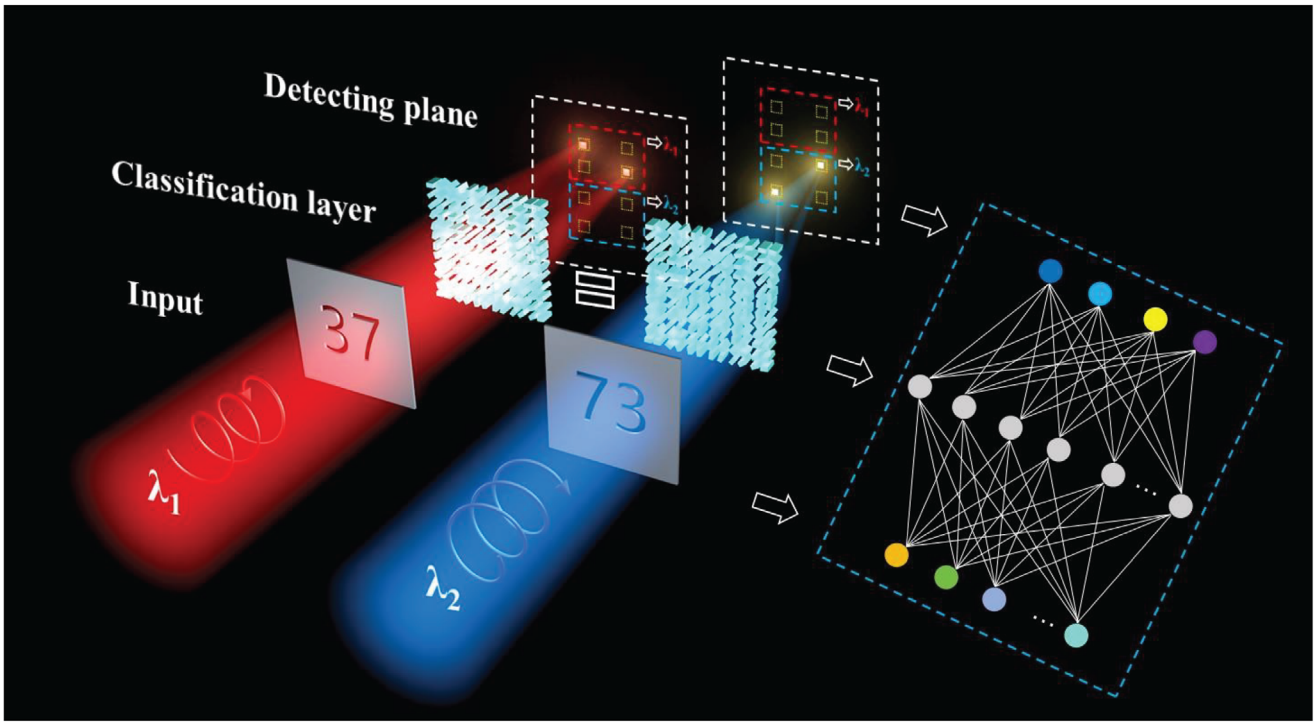

Figure 1. Schematic of multi-wavelength and multi-target DNNs (M_wM_t-DNNs). The functionalities of multi-wavelength and multi-target digital recognition are integrated into a single metasurface, which can be considered as a hidden layer. For the input of a dual digital image at two different wavelengths, the recognition of wavelength, two digits and spatial sequence (the sequential order of the two digits) can be realized by focusing the incident light into specified regions.

and ultra-compact platform for mimicking DNNs with unconventional functionalities. Currently, significant progress has been made in optical analog computing based on metasurfaces, including integrator, convolutional operator, differentiator, and equation solver.[44–51] However, the current DNN devices are primarily designed for classifying a single target at a specific frequency. Multi-wavelength and multi-target recognition provides a more detailed understanding of environments, making it more attractive for advanced practical applications.

Nonetheless, to tackle the above challenges, we propose a metasurface approach that integrates DNNs with various functionalities into a multichannel metasurface, enabling the mimicry of multi-wavelength and/or multi-target DNNs with multiple functions. By training a single target at different wavelengths and integrating phase requirements into a single-layer metasurface, multi-wavelength DNNs (M_w-DNNs) are constructed to simultaneously classify wavelength and target. The multi-target DNNs (M_t-DNNs) for classifying multiple targets and spatial sequences can be realized by encoding different phase profiles into a metasurface. Furthermore, multi-wavelength and multi-target DNNs (M_wM_t-DNNs) are designed to simultaneously classify wavelengths, multiple targets, and spatial sequences by integrating these functionalities into the orthogonal helical channels of a metasurface. This robust approach not only enables improved processing capacity and reduced computer resource consumption but also opens an avenue for developing integrated DNNs and artificial intelligence systems.

2. Design Methodology

Figure 1 illustrates a multiplexed DNN that can recognize digital images at multiple wavelengths using a single-layer metasurface. The input layer consists of two digits (e.g., "37" or "73") that are processed by a hidden layer containing many neurons with different phase profiles. The output layer has eight detection areas. When a left circularly polarized (LCP) terahertz beam with a wavelength λ_1 shines on the digits "37", the diffractive field is modulated by the neurons in the hidden layer, and then focused onto specific regions of the detection plane (red dashed boxes). Conversely, when a right circularly polarized (RCP) terahertz beam with a wavelength λ_2 shines on the digits "73", the transmitted waves are also modulated by the same neurons, resulting in focused field distributions on different regions of the detection plane (blue dashed boxes). The detection plane has four rows and two columns of discrete regions designed to simultaneously recognize the wavelength and spatial sequence of the incident digits. The wavelength can be identified by detecting the focusing light beams in the regions outlined with red or blue dashed boxes (λ_1 for red, λ_2 for blue). Additionally, the spatial sequence of the incident digits is determined by the focused field in antidiagonal or diagonal detection areas (e.g., "37" with an antidiagonal focus and "73" with a diagonal focus).

The DNNs for recognizing a digit at a pre-designed wavelength (λ_1 or λ_2) are trained based on the optical diffraction theory. This approach enables the realization of multiplexed DNNs by integrating different tasks, such as multi-wavelength and

multi-target digital recognition, into separate channels within a geometric metasruface. According to the Huygens–Fresnel principle, each point on the wavefront can be considered as a secondary spherical source that forms a new wavefront at the next moment based on interference. This means that each meta-atom in the geometric metasurface can be viewed as an optical neuron (that is a monopole source) connected to neurons in preceding and following layers through diffraction. Based on the Rayleigh–Sommerfeld diffraction theory, the underlying physics of DNNs can be analyzed by examining the connection between the complex field $U(r^l)$ from the lth layer and $U(r^{l+1})$ from the $(l+1)th$ layer, which is described by the following equation:

$$U(r^{l+1}) = t(r') \int\int_s U(r^l) \cdot h(r^{l+1} - r^l) dxdy \quad (1)$$

The complex field $U(r^l)$ is transmitted after the digital mask, where l is defined as 1 ($l = 1$) in this work. Additionally, the complex field ($U(r^{l+1})$) is manipulated by a spatially varying complex transmittance $t(r')$ expressed as $t(r') = A^l e^{i\gamma^l}$, where A^l is the amplitude and γ^l is the phase. The impulse response $h(r^{l+1} - r^l)$ is defined as follows:

$$h(r^{l+1} - r^l) = \frac{z^{l+1} - z^l}{R^2}\left(\frac{1}{2\pi R} - \frac{1}{j\lambda}\right)\exp\left(j\frac{2\pi R}{\lambda}\right) \quad (2)$$

where λ is the incident wavelength, $R = \sqrt{(x^{l+1} - x_i^l)^2 + (y^{l+1} - y_i^l)^2 + (z^{l+1} - z_i^l)^2}$, and $j = \sqrt{-1}$. Then, we construct the forward propagation model of DNN using a loss function and a stochastic gradient descent approach. Specifically, the loss function is defined as the mean squared error (MSE) to evaluate the difference between the input signal and the detector output. Meanwhile, the stochastic gradient descent algorithm is employed for iterative training to achieve the desired output. Further details on model training, derivation, and integration of multiplexed DNN with multiple functionalities are provided in Section S1 (Supporting Information). For machine learning, we utilize classical datasets from the Modified National Institute of Standards and Technology (MNIST). The detection plane is divided into a variety of discrete sub-regions to serve as the physical plane of network output for recognizing identified objects. More detailed model training and derivation are described in the Experimental Section.

To demonstrate multiplexed DNNs with multi-wavelength and/or multi-target digital recognition, we design multichannel metasurfaces comprising various anisotropic meta-atoms with identical shapes but different in-plane orientations (**Figure 2**a,b). Each meta-atom is optimized to be a quasi-half-wave plate, resulting in structural parameters of $L = 112$ μm, $W = 33$ μm, $H_1 = 500$ μm, $H_2 = 500$ μm, and $P = 130$ μm in the x and y directions. By rotating each meta-atom in its in-plane orientation, the Pancharatnam-Berry phase modulation mechanism provides an angle-dependent full phase range of $[0, 2\pi]$ for circularly polarized EM waves. In Figure 2c (top figure) for the incidence of y-polarized (TE) or x-polarized (TM) THz waves, the transmittance at 0.52 THz is nearly 95%, with a phase difference between transmitted TE and TM modes of nearby π. When an optimized meta-atom is illuminated by LCP THz waves, the polarization conversion efficiency (defined as the ratio between the power of transmitted cross-polarized THz waves and incident power) at 0.52 THz is nearly 88%, as shown in Figure 2c (bottom figure). Figure 2d–f shows the fabricated samples for recognizing a single digit at two wavelengths, classifying two digits and spatial sequence at one wavelength, and recognizing two digits and spatial sequence at two wavelengths, respectively. The characteristics of our fabricated samples are experimentally demonstrated by near-field scanning terahertz microscopy (NSTM), as shown in Figure 2g. The femtosecond laser beam is split into two parts: one part generates terahertz (THz) radiation through a photoconductive antenna, while the other part is coupled with a THz tip to detect field distributions after the fabricated samples. Further details on the experimental setup can be found in the Experimental Section.

3. Results

For a proof-of-concept implementation, an all-dielectric single-layer geometric metasurface is theoretically designed and experimentally demonstrated to integrate DNNs with single-digit recognition at two wavelengths, as shown in **Figure 3**. To demonstrate multiwavelength digit identification, classical datasets from the Modified National Institute of Standards and Technology (MNIST) are used for machine learning. The digits 3 and 7 are exploited to demonstrate the Mw-DNNs. The design process is schematically shown in Figure 3a. Neural networks for dual-class object recognition are independently trained at 0.52 and 0.6 THz with 100 × 100 neurons (10 000 in total), and the layer-to-layer axial distance is fixed at 10 mm. The training convergence of MNIST with respect to epoch number is given in Section S2 (Supporting Information). After training the digits 3 and 7 at both wavelengths, phase distributions are obtained for each wavelength. These profiles are shown in Figure 3a. By integrating the two phase-profiles into a geometric metasurface, the Mw-DNNs for recognizing a digit at two wavelengths can be achieved. This realization enables us to express the corresponding phase requirement for the geometric metasurface as follows:

$$\Phi_{mw} = \arg[\exp(i\phi_{LCP}) + \exp(i\phi_{RCP})] \quad (3)$$

where $\phi_{LCP} = -\phi_{\lambda_1}$ and $\phi_{RCP} = \phi_{\lambda_2}$. It should be noted that the trained phase profiles at 0.52 and 0.6 THz are respectively encoded into the LCP and RCP channels of a geometric metasurface, resulting in the Mt-DNNs with multi-wavelength digit recognition. The fundamental principle for the superposition of multiple functions at multi-wavelength with a uniform geometric metasurface is discussed in Section S3 (Supporting Information). The physical plane of the designed network output is divided into four discrete detection regions to simultaneously identify the digits and incident wavelengths. As shown in Figure 3b,c for the incidence of LCP THz waves at 0.52 THz, the calculated field distributions in the detection plane are located at the top left/right corner for the handwritten digit 7/3, respectively. In contrast, for the digits "7" and "3", under the illumination of RCP THz waves at 0.6 THz, the output diffraction field distributions are focused at the bottom left and bottom right corners, respectively (Figure 3d,e). The calculated energy distributions are shown in Figure 3f, which clearly shows

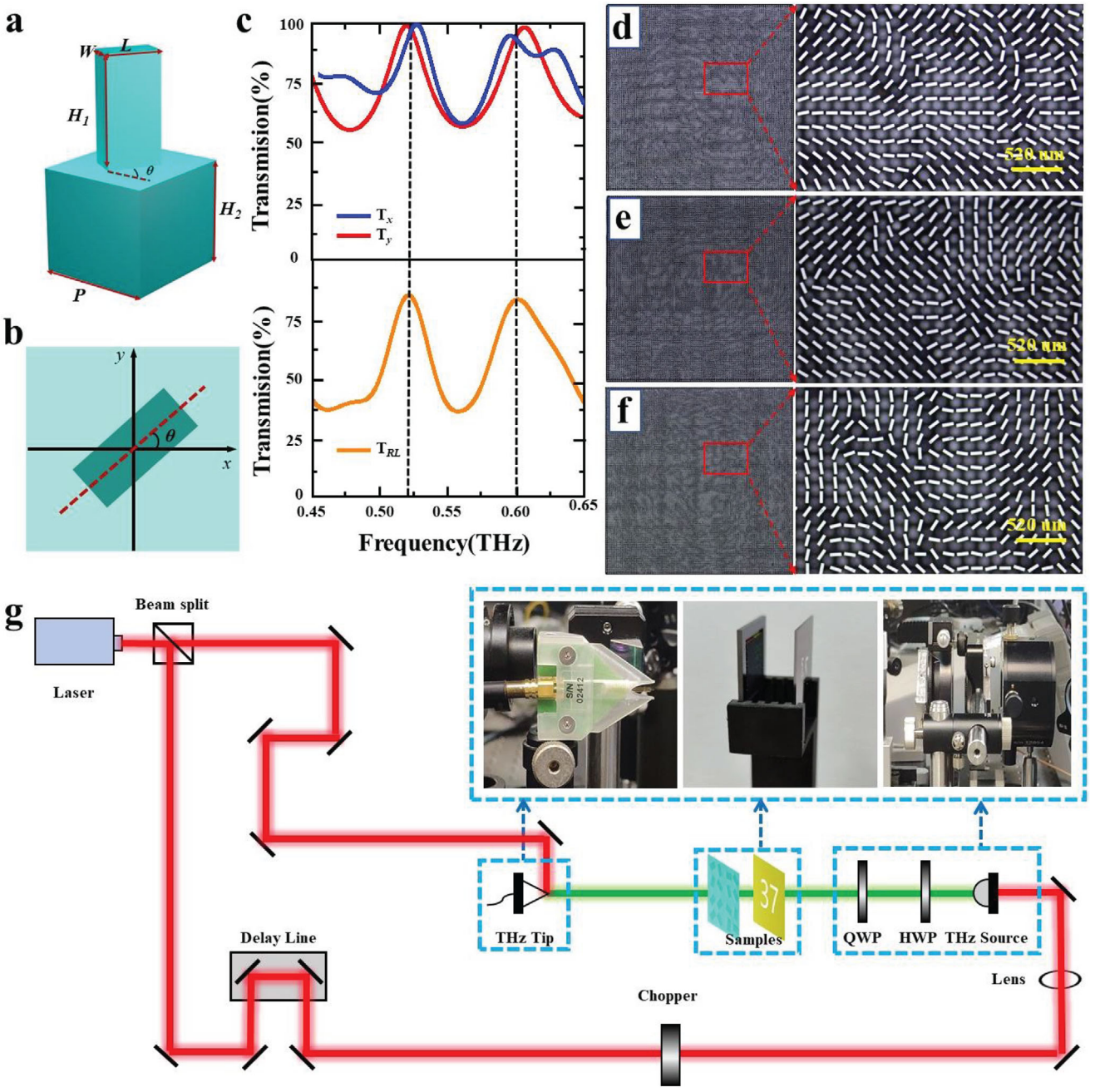

Figure 2. Metasurface design and experimental setup. a,b) Schematics of a meta-atom fabricated on a silicon substrate. *L*, *W*, and H_1 are the length, width, and height of meta-atom, respectively. *P* is the period and H_2 is the height of the substrate. c) The transmission spectra (top) of a meta-atom under the illumination of *x*-polarized (blue curve) and *y*-polarized (red curve) THz waves. The polarization conversion efficiency is defined as the ratio between the transmitted RCP THz waves and the incident LCP THz waves, which is shown in the orange curve (bottom). The optical images of fabricated samples can classify a singletarget at two-wavelengths d), two-targets at a singlewavelength e), and two-targets at two-wavelengths f), respectively. g) The experimental setup for demonstrating the multiplexed DNNs.

that the designed metasurface can simultaneously identify handwritten digits and incident wavelengths. In the experiment, the handwritten digits are fabricated based on film deposition and ultrasonic stripping. Under the illumination of LCP THz waves at 0.52 THz, the output field distributions are located at the top left/right corner for the handwritten digit 7/3, as shown in Figure 3b,c. For the incidence of RCP THz waves at 0.6 THz, the measured field distributions in the detection plane are focused at the bottom left/right corner for the handwritten digit 7/3, as demonstrated in Figure 3d,e. Figure 3g shows the measured energy distributions, which demonstrate the capability of the recognition of digits and wavelengths. The test results for identified and misidentified instances of simulation and experiment are demonstrated using the confusion matrix, as shown

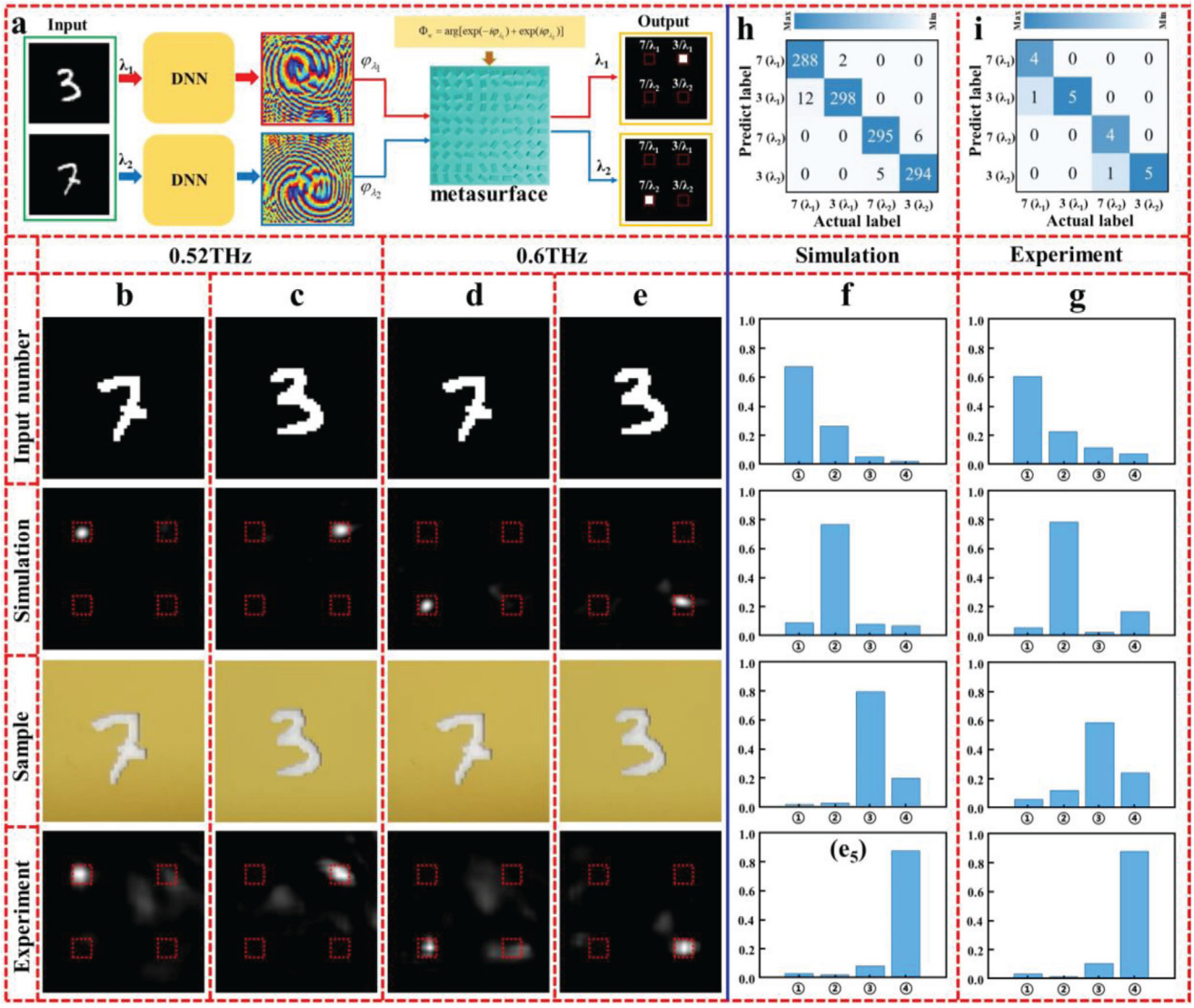

Figure 3. Calculated and experimental results of multi-wavelength DNNs (M_w-DNNs). a) Flowchart of M_w-DNN design: the digits "3" and "7" are independently trained at λ_1 and λ_2, and then the phase requirements are encoded into a single-layer metasurface to realize a multi-wavelength digit-classifier. Calculated and measured output-field intensity-distributions for b) the digit of "7" at 0.52 THz, c) the digit of "3" at 0.52 THz, d) the digit of "7" at 0.6 THz, and e) the digit of "3" at 0.6 THz. f) Calculated and g) measured output-energy distribution maps. h,i) Calculated and measured confusion matrices for the designed M_w-DNN. The labels of ①–④ correspond to the detection regions with the spatial sequences ranging from left to right and from top to bottom.

in Figure 3h,i. The test accuracy achieves 97.5%/90% for numerical/experimental statistical results. The experimental results agree well with the numerical simulations, except for a slightly lower accuracy which can be attributed to experimental errors. The detailed discussions for alignment errors of M_w-DNNs are given in Section S4 (Supporting Information). In addition to recognizing handwritten digits, this approach can also be applied to realize fashion classification, as shown in Section S5 (Supporting Information). Such a multichannel metasurface can also integrate DNNs for the recognition of digits and fashions at different wavelengths, implying that our proposed approach can simultaneously recognize digits, fashions, and wavelengths (Section S6 (Supporting Information)). The detailed discussions of the crosstalk between the two polarization channels (for the recognition of a single digit) without wavelength difference are given in Section S7 (Supporting Information). In addition, the more numbers of classifications in a single channel or dual channels are numerically demonstrated in Section S8 (Supporting Information).

The existing architectures of DNNs for digit or fashion identification are limited to recognizing a single target, which cannot showcase unprecedented capabilities in massively parallel processing. Therefore, identifying multiple targets (defined as parallel processing) is highly desirable. As the number of targets increases, the multi-target DNNs (Mt- DNNs) are developed to recognize the multiple targets and the spatial sequence of each

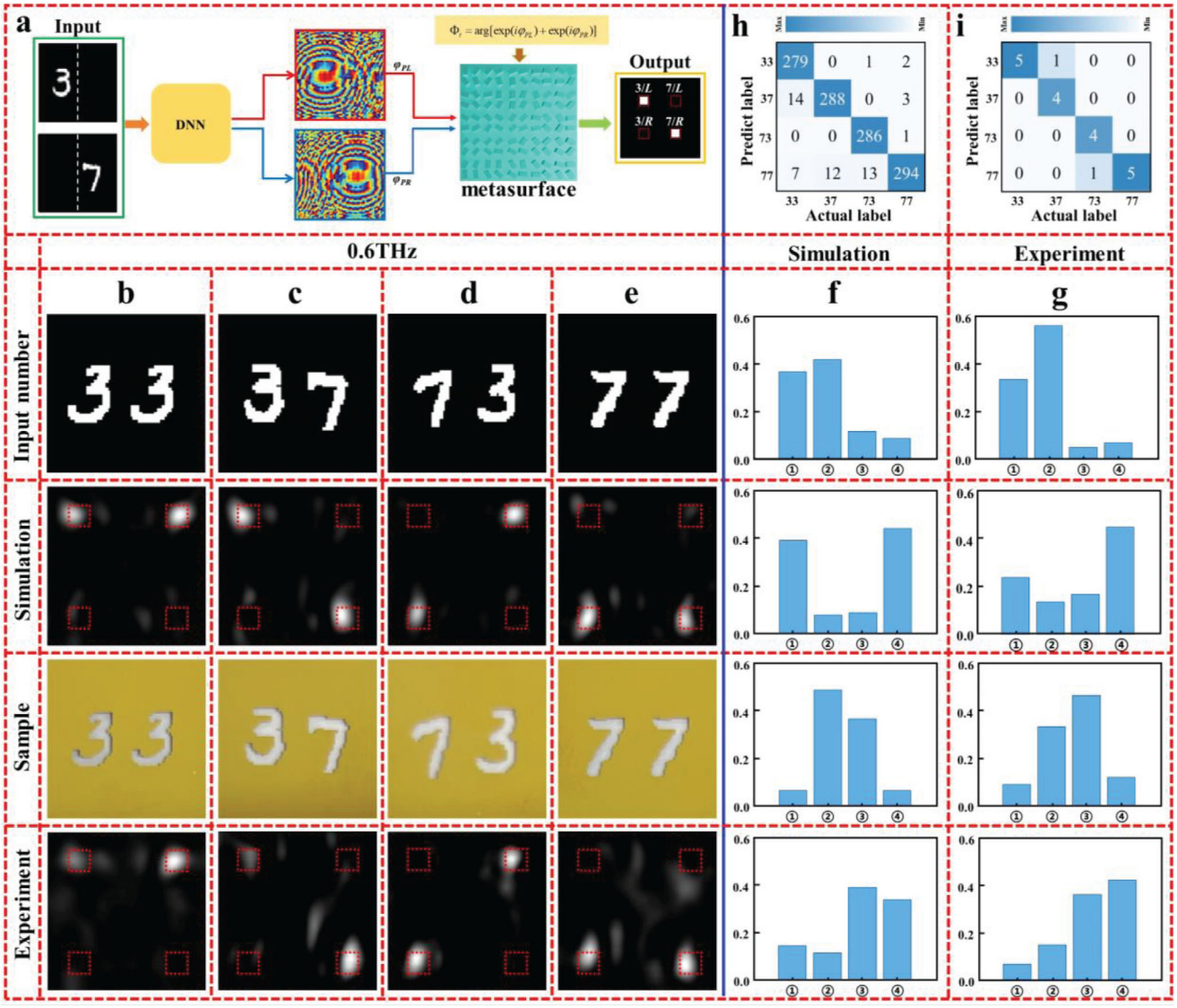

Figure 4. Calculated and experimental results of multi-target DNNs (M_t-DNNs). a) Flowchart of M_t-DNN design: the digits "3" and "7" are independently trained at left and right half-space, and then the phase requirements are encoded into a single-layer metasurface to realize a multi-target digit-classifier. Calculated and measured output-field intensity-distributions for b) the digits of "33" at 0.6 THz, c) the digits of "37" at 0.6 THz, d) the digits of "73" at 0.6 THz, and e) the digit of "77" at 0.6 THz. f) Calculated and g) measured output-energy distribution maps. h,i) Calculated and measured confusion matrices for the designed M_w-DNN. The labels of ①–④ correspond to the detection regions with the spatial sequences ranging from left to right and from top to bottom.

target. For instance, two targets of "3" and "7" can be composed into "37" and "73", which are two different values. To simultaneously identify each target ("37" or "73") and the sequential order of these two digits is crucial. **Figure** 4a illustrates the flow chart for designing Mt-DNNs based on metasurfaces to demonstrate a multi-target classifier. The input mask is divided into two regions, namely the left half-space and right half-space. The training convergence of MNIST with respect to epoch number is provided in Section S2 (Supporting Information). After training the digits located at the left half-space and right half-space, two-phase profiles are obtained and then integrated into a single metasurface to mimick the Mt-DNNs for recognizing multiple targets and sequential order recognition. The encoded phase profile in such a metasurface can be expressed as:

$$\Phi_{mt} = \arg[\exp(i\phi_{PL}) + \exp(i\phi_{PR})] \quad (4)$$

where ϕ_{PL} is the trained phase for identifying the target at the left half-space, while ϕ_{PR} is the trained phase for identifying the target at the right half-space. Figure 4b (the top two figures) numerically illustrates handwritten digits and output diffraction field distributions for THz waves at 0.6 THz. The focused electric-field distributions primarily occur at the top left and top right corners, demonstrating double digits of "33". For handwritten digits

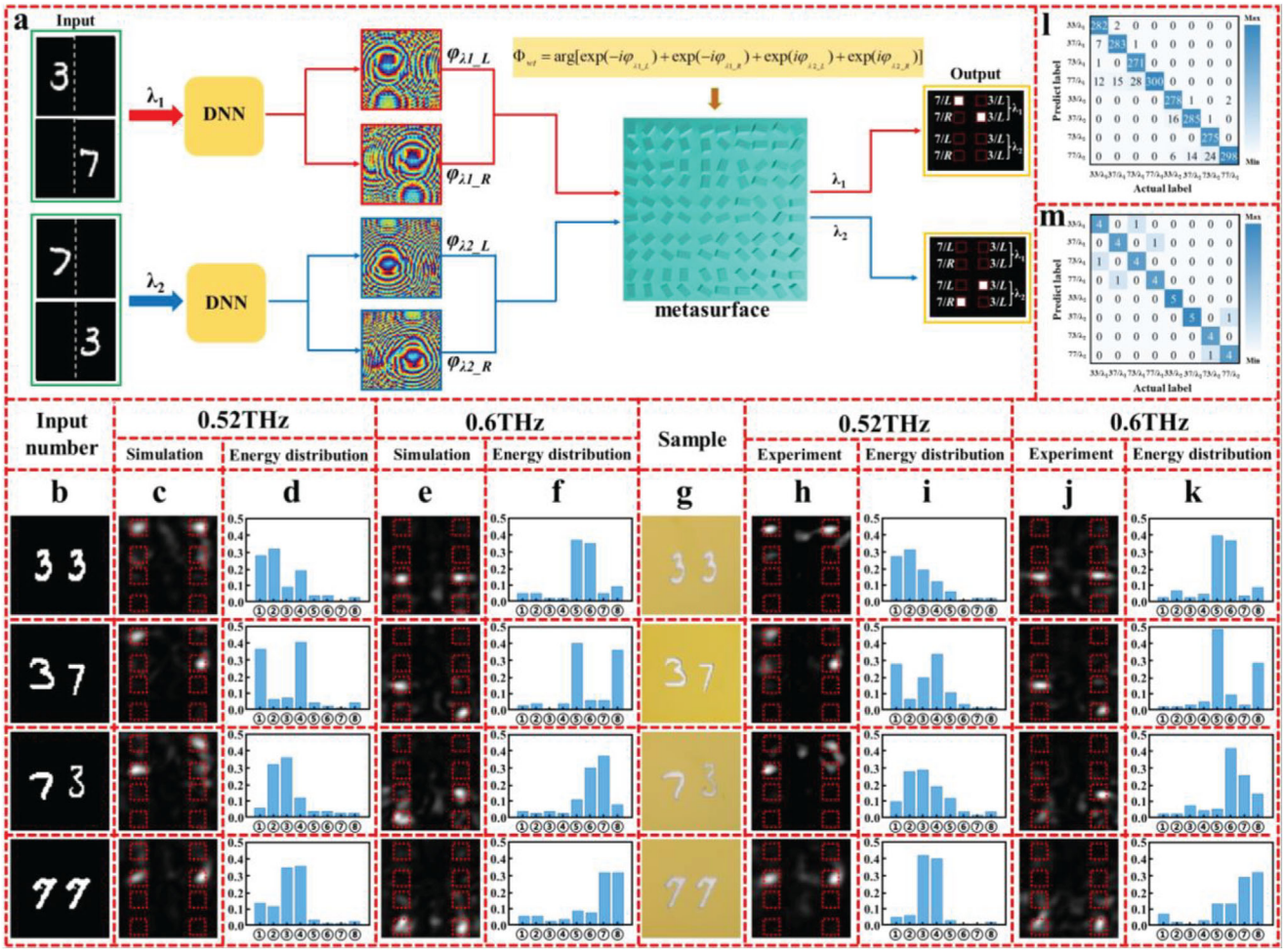

Figure 5. Calculated and experimental results of multi-wavelength and multi-target DNNs (M_wM_t-DNNs). a) Flowchart of M_wM_t-DNN design: the digits "3" and "7" are independently trained at left and right half-space and different wavelengths of λ_1 and λ_2, and then the phase requirements are encoded into a single-layer metasurface to realize a multi-wavelength and multi-target digit-classifier. b,g) The input dual-digits. c,e) Calculated and h,j) measured output-field intensity-distributions. d,f) Calculated and i,k) measured output-energy distribution maps. l,m) Calculated and measured confusion matrices for the designed MM-DNN. The labels of ①–⑧ correspond to the detection regions with the spatial sequences ranging from left to right and from top to bottom.

"37", "73", and "77", the calculated diffractive fields in the detection plane are focused at antidiagonal, diagonal, and bottom corners (Figure 4c–e), respectively. Fabricated masks and measured diffractive field distributions are shown in Figure 4b–e. Calculated and measured energy distributions are illustrated in Figure 4f,g, demonstrating the designed metasurface's ability to simultaneously recognize digits and their corresponding sequential order. The test accuracy reaches 97.9% and 90% between numerical simulations and measurements, as shown in Figure 4h,i. This Mt-DNN can be extended to recognize multiple fashions or hybrid targets between digits and fashions, with their sequential order discussed in Sections S9 and S10 (Supporting Information). The crosstalk for the input digits in the left/right half-space using the phases in classifying digits in the right/left half space and the only one phase training for the recognition of dual digits are given in Section S11 (Supporting Information).

Furthermore, our proposed approach can be extended to realize a multi-target and multi-wavelength classifier (or M_wM_t-DNN). The flow chart for the design of a geometric metasurface that can simultaneously recognize multiple digits at multiple wavelengths is shown in **Figure 5a**. The input mask is divided into left and right half spaces, with targets trained independently at two wavelengths in these regions. For dual-target recognition at two wavelengths, four-phase profiles are obtained after training, which are then encoded into a geometric metasurface as follows:

$$\Phi_{mt-mw} = \arg[\exp(-i\varphi_{\lambda1\_L}) + \exp(-i\varphi_{\lambda1\_R}) + \exp(i\varphi_{\lambda2\_L}) + \exp(i\varphi_{\lambda2\_R})] \quad (5)$$

where the phase profiles ($\varphi_{\lambda1\_L}$, $\varphi_{\lambda1\_R}$) at λ_1 (0.52 THz) are integrated into the LCP channel while phase profiles ($\varphi_{\lambda2\_L}$, $\varphi_{\lambda2\_R}$) at λ_2 (0.6 THz) are encoded into the RCP channel. The training convergence of MNIST versus epoch number is provided in Section S2 (Supporting Information). For the input digits "33" under

the illumination of LCP THz waves at 0.52 THz, the diffractive fields at the detection plane are focused on the top left and top right corners, as shown in Figure 5b,c (the top two figures). Our designed metasurface enables recognition of handwritten digits "37", "73" and "77" at this wavelength, as numerically demonstrated in Figure 5c. The energy distributions shown in Figure 5d are consistent with our predesigned results. When the incident frequency is switched to 0.6 THz, our metasurface can identify dual digits and their corresponding spatial sequence, as depicted in Figure 5e,f. The fabricated samples are presented in Figure 5g, while the measured results are shown in Figure 5h–k which are in agreement with our simulated results. Figure 5l,m display numerical and measured confusion matrices, demonstrating test accuracy of 94.6% and 85%, respectively, for statistical results. The detailed discussions of the crosstalk between the two helical channels (for the recognition of dual-digit) without wavelength difference are given in Section S7 (Supporting Information).

4. Conclusion

Different from the typical demonstration of neural networks with novel functionalities that involve 3D printing devices or propagation-phase-based meta-devices, this work aims to mimick multiplexed DNNs with unprecedented capabilities in massively parallel processing with a compact metasurface platform. By training each target at different wavelengths and multiplexing various functions into single or dual helical channels of the metasurface, we have demonstrated the recognition of a single target at two wavelengths, two targets at a single wavelength, and two targets at two wavelengths. Our designed DNNs consist of a single hidden layer realized with a single-layer geometric metasurface, exhibiting unprecedented capabilities in identifying digits, fashions, wavelengths, and spatial sequences between multiple targets. This multiplexed DNN architecture opens up new possibilities for further integrating versatile functions into multichannel metasurfaces. To quantify the match between numerical testing results and experimental demonstrations, 80 samples (i.e., 20 samples for single digits and 60 samples for dual-digit) are fabricated as input masks in this work. The test accuracy experiment is relatively smaller than that in numerical simulation. We acknowledge that the more samples, the higher the accuracy in the test accuracy, and we utilize a moderate approach, i.e., five different inputs per digit/dual-digit, to experimentally demonstrate the test accuracy. Although the test accuracy in the experiment is relatively smaller than that in numerical simulation, they are generally demonstrated the recognition rates of our fabricated metasurfaces in mimicking multi-target and multi-wavelength DNNs. Furthermore, designing multi-layer meta-neurons could enable more complex recognition tasks or higher classification accuracy. The robust approach presented here can also be extended to design reconfigurable DNNs based on tunable meta-devices realized by phase-change materials, liquid crystals, and other technologies.

In summary, a metasurface approach is proposed to realize multiplexed DNNs (e.g., Mw-DNNs, Mt-DNNs, and MwMt-DNNs) that can process multiple tasks in parallel. To validate this concept, we have designed and fabricated a single-layer geometric metasurface capable of recognizing a single target at two wavelengths, two targets at one wavelength, and two targets at two wavelengths. Unlike traditional DNNs with a single function in classifying digits or fashions, our proposed multiplexed-DNNs can not only classify these patterns but also identify the corresponding wavelength and spatial sequence between multiple targets. This versatile approach may have potential applications in high-speed parallel computing and multi-skilled artificial intelligence systems.

5. Experimental Section

Training: The design of a single-layer diffractive neural network was performed using Python (v3.9.16) and TensorFlow (v2.6.0, Google Inc.) on a Windows 10 operating system (Microsoft) with 2 × Intel(R) Xeon(R) CPU E5-2696 v4 @2.20 GHz central processing unit (CPU, Intel Inc.), 192 GB of RAM, and a GeForce RTX 4080 Ti graphical processing unit (GPU, Nvidia Inc.). The MNIST and Fashion-MNIST datasets are used for training with a batch size of 8, over 10 epochs, and a learning rate of 0.005. The mean square error was employed as the loss function for training the MNIST datasets, and the desired phases of a hidden layer for network training are updated based on the stochastic gradient descent algorithm.

Experimental Setup: To detect the electric-field intensity distributions after the fabricated samples, a Near-Field Scanning Terahertz Time-Domain Spectrum Microscopy System (NSTDSM) was established, as shown in Figure 2g. A femtosecond laser with a central wavelength of 780 nm was divided into two parts. One part of the laser beam was guided into the photoconductive antenna emitter to generate THz waves for the characterization of the designed sample. Simultaneously, the other part of the laser beam was coupled into a single-mode fiber (with a length of 10 cm) and shines on the THz tip. The THz tip was mounted on a 3D translation stage to detect the electric-field intensity distributions. The position of fabricated samples is fixed, while the electric-field distributions are obtained by shifting the THz tip.

Supporting Information

Supporting Information is available from the Wiley Online Library or from the author.

Acknowledgements

X.Z. and Y.Z. acknowledge the National Natural Science Foundation of China (61988102, 62271320, and 61871268), "Shuguang" Program of Shanghai Education Commission (19SG44), the Science and Technology Commission of Shanghai Municipality (21S31907400), and the Shanghai Municipal Science and Technology Commission (22JC1400200). X.C. acknowledges the Leverhulme Trust (RPG-2023-283 and RPG-2021-145).

Conflict of Interest

The authors declare no conflict of interest.

Author Contributions

X.Z., X.C., and Y.Z. initiated the idea. H.C. conducted the numerical simulations. H.C. and T.Z. performed the measurements. X.Z. and X.C. prepared the manuscript. X.Z. and Y.Z. supervised the project. All the authors discussed and analyzed the results.

Data Availability Statement

The data that support the findings of this study are available in the supplementary material of this article.

Keywords

diffraction neural networks, metasurface, multi-target and multi-wavelength recognition, parallel processing

Received: August 6, 2024
Published online:

[1] K. He, X. Zhang, S. Ren, J. Sun, *IEEE Trans. Pattern Anal. Mach. Intell.* **2015**, *37*, 1904.
[2] S. Bach, A. Binder, G. Montavon, F. Klauschen, K.-R. Müller, W. Samek, *PLoS One* **2015**, *10*, e0130140.
[3] W. Liu, Z. Wang, X. Liu, N. Zeng, Y. Liu, F. E. Alsaadi, *Neurocomputing* **2017**, *234*, 11.
[4] B. Shi, X. Bai, C. Yao, *IEEE Trans. Pattern Anal. Mach. Intell.* **2017**, *39*, 2298.
[5] Y. Shen, N. C. Harris, S. Skirlo, M. Prabhu, T. Baehr-Jones, M. Hochberg, X. Sun, S. Zhao, H. Larochelle, D. Englund, M. Soljačić, *Nature Photon.* **2017**, *11*, 441.
[6] A. Krizhevsky, I. Sutskever, G. E. Hinton, *Commun. ACM* **2017**, *60*, 84.
[7] K. He, X. Zhang, S. Ren, J. Sun, in *2016 IEEE Conf. on Computer Vision and Pattern Recognition (CVPR)*, IEEE, Las Vegas, NV, USA **2016**, pp. 770–778.
[8] T. N. Sainath, A. Mohamed, B. Kingsbury, B. Ramabhadran, in *2013 IEEE International Conference on Acoustics, Speech and Signal Processing*, IEEE, Vancouver, BC, Canada **2013**, pp. 8614–8618.
[9] G. Hinton, L. Deng, D. Yu, G. Dahl, A. Mohamed, N. Jaitly, A. Senior, V. Vanhoucke, P. Nguyen, T. Sainath, B. Kingsbury, *IEEE Signal Process. Mag.* **2012**, *29*, 82.
[10] T. Young, D. Hazarika, S. Poria, E. Cambria, *IEEE Comput. Intell. Mag.* **2018**, *13*, 55.
[11] G. Wetzstein, A. Ozcan, S. Gigan, S. Fan, D. Englund, M. Soljačić, C. Denz, D. A. B. Miller, D. Psaltis, *Nature* **2020**, *588*, 39.
[12] G. Genty, L. Salmela, J. M. Dudley, D. Brunner, A. Kokhanovskiy, S. Kobtsev, S. K. Turitsyn, *Nat. Photonics* **2021**, *15*, 91.
[13] H. Zhou, J. Dong, J. Cheng, W. Dong, C. Huang, Y. Shen, Q. Zhang, M. Gu, C. Qian, H. Chen, Z. Ruan, X. Zhang, *Light: Sci. Appl.* **2022**, *11*, 30.
[14] J. Liu, Q. Wu, X. Sui, Q. Chen, G. Gu, L. Wang, S. Li, *PhotoniX* **2021**, *2*, 5.
[15] X. Y. Liu, M. K. Chen, D. P. Tsai, *Laser Photon. Rev.* **2024**, *18*, 2300456.
[16] X. Lin, Y. Rivenson, N. T. Yardimci, M. Veli, Y. Luo, M. Jarrahi, A. Ozcan, *Science* **2018**, *361*, 1004.
[17] M. K. Chen, X. Y. Liu, Y. N. Sun, D. P. Tsai, *Chem. Rev.* **2022**, *122*, 15356.
[18] C. Qian, X. Lin, X. Lin, J. Xu, Y. Sun, E. Li, B. Zhang, H. Chen, *Light: Sci. Appl.* **2020**, *9*, 59.
[19] M. Veli, D. Mengu, N. T. Yardimci, Y. Luo, J. Li, Y. Rivenson, M. Jarrahi, A. Ozcan, *Nat. Commun.* **2021**, *12*, 37.
[20] P. Wang, W. Xiong, Z. Huang, Y. He, Z. Xie, J. Liu, H. Ye, Y. Li, D. Fan, S. Chen, *Photonics Res.* **2021**, *9*, 2116.
[21] Z. Huang, Y. He, P. Wang, W. Xiong, H. Wu, J. Liu, H. Ye, Y. Li, D. Fan, S. Chen, *Opt. Express* **2022**, *30*, 5569.
[22] J. Li, Y.-C. Hung, O. Kulce, D. Mengu, A. Ozcan, *Light: Sci. Appl.* **2022**, *11*, 153.
[23] Z. Liu, Z. Li, Z. Liu, J. Li, H. Cheng, P. Yu, W. Liu, C. Tang, C. Gu, J. Li, S. Chen, J. Tian, *Adv. Funct. Mater.* **2015**, *25*, 5428.
[24] Y. Deng, C. Wu, C. Meng, S. I. Bozhevolnyi, F. Ding, *ACS Nano* **2021**, *15*, 18532.
[25] W. Li, B. Chen, X. Hu, H. Guo, S. Wang, J. Wu, K. Fan, C. Zhang, H. Wang, B. Jin, J. Chen, P. Wu, *Sci. Adv.* **2023**, *9*, eadi7565.
[26] N. K. Grady, J. E. Heyes, D. R. Chowdhury, Y. Zeng, M. T. Reiten, A. K. Azad, A. J. Taylor, D. A. R. Dalvit, H.-T. Chen, *Science* **2013**, *340*, 1304.
[27] L. Cong, N. Xu, J. Gu, R. Singh, J. Han, W. Zhang, *Laser Photon. Rev.* **2014**, *8*, 626.
[28] X. Zang, F. Dong, F. Yue, C. Zhang, L. Xu, Z. Song, M. Chen, P. Chen, G. S. Buller, Y. Zhu, S. Zhuang, W. Chu, S. Zhang, X. Chen, *Adv. Mater.* **2018**, *30*, 1707499.
[29] F. Yue, D. Wen, J. Xin, B. D. Gerardot, J. Li, X. Chen, *ACS Photonics* **2016**, *3*, 1558.
[30] H. Ahmed, Y. Intaravanne, Y. Ming, M. A. Ansari, G. S. Buller, T. Zentgraf, X. Chen, *Adv. Mater.* **2022**, *34*, 2203044.
[31] Y. Ming, Y. Intaravanne, H. Ahmed, M. Kenney, Y. Lu, X. Chen, *Adv. Mater.* **2022**, *34*, 2109714.
[32] X. Chen, L. Huang, H. Mühlenbernd, G. Li, B. Bai, Q. Tan, G. Jin, C.-W. Qiu, S. Zhang, T. Zentgraf, *Nat. Commun.* **2012**, *3*, 1198.
[33] M. Khorasaninejad, W. T. Chen, R. C. Devlin, J. Oh, A. Y. Zhu, F. Capasso, *Science* **2016**, *352*, 1190.
[34] S. Wang, P. C. Wu, V.-C. Su, Y.-C. Lai, C. Hung Chu, J.-W. Chen, S.-H. Lu, J. Chen, B. Xu, C.-H. Kuan, T. Li, S. Zhu, D. P. Tsai, *Nat. Commun.* **2017**, *8*, 187.
[35] W. T. Chen, A. Y. Zhu, V. Sanjeev, M. Khorasaninejad, Z. Shi, E. Lee, F. Capasso, *Nature Nanotech.* **2018**, *13*, 220.
[36] R. J. Lin, V.-C. Su, S. Wang, M. K. Chen, T. L. Chung, Y. H. Chen, H. Y. Kuo, J.-W. Chen, J. Chen, Y.-T. Huang, J.-H. Wang, C. H. Chu, P. C. Wu, T. Li, Z. Wang, S. Zhu, D. P. Tsai, *Nat. Nanotechnol.* **2019**, *14*, 227.
[37] X. Zang, H. Ding, Y. Intaravanne, L. Chen, Y. Peng, J. Xie, Q. Ke, A. V. Balakin, A. P. Shkurinov, X. Chen, Y. Zhu, S. Zhuang, *Laser Photon. Rev.* **2019**, *13*, 1900182.
[38] L. Huang, X. Chen, H. Mühlenbernd, H. Zhang, S. Chen, B. Bai, Q. Tan, G. Jin, K.-W. Cheah, C.-W. Qiu, J. Li, T. Zentgraf, S. Zhang, *Nat. Commun.* **2013**, *4*, 2808.
[39] D. Wen, F. Yue, G. Li, G. Zheng, K. Chan, S. Chen, M. Chen, K. F. Li, P. W. H. Wong, K. W. Cheah, E. Yue Bun Pun, S. Zhang, X. Chen, *Nat. Commun.* **2015**, *6*, 8241.
[40] G. Zheng, H. Mühlenbernd, M. Kenney, G. Li, T. Zentgraf, S. Zhang, *Nature Nanotech.* **2015**, *10*, 308.
[41] L. Jin, Z. Dong, S. Mei, Y. F. Yu, Z. Wei, Z. Pan, S. D. Rezaei, X. Li, A. I. Kuznetsov, Y. S. Kivshar, J. K. W. Yang, C.-W. Qiu, *Nano Lett.* **2018**, *18*, 8016.
[42] Q. Dai, Z. Guan, S. Chang, L. Deng, J. Tao, Z. Li, Z. Li, S. Yu, G. Zheng, S. Zhang, *Adv. Funct. Mater.* **2020**, *30*, 2003990.
[43] S. So, J. Kim, T. Badloe, C. Lee, Y. Yang, H. Kang, J. Rho, *Adv. Mater.* **2023**, *35*, 2208520.
[44] X. Luo, Y. Hu, X. Ou, X. Li, J. Lai, N. Liu, X. Cheng, A. Pan, H. Duan, *Light: Sci. Appl.* **2022**, *11*, 158.
[45] C. He, D. Zhao, F. Fan, H. Zhou, X. Li, Y. Li, J. Li, F. Dong, Y.-X. Miao, Y. Wang, L. Huang, *Opto-Electron. Adv.* **2024**, *7*, 230005.
[46] H. Babashah, Z. Kavehvash, S. Koohi, A. Khavasi, *J. Opt. Soc. Am. B* **2017**, *34*, 1270.
[47] W. Fu, D. Zhao, Z. Li, S. Liu, C. Tian, K. Huang, *Light: Sci. Appl.* **2022**, *11*, 62.
[48] J. Sol, D. R. Smith, P. Del Hougne, *Nat. Commun.* **2022**, *13*, 1713.
[49] N. Mohammadi Estakhri, B. Edwards, N. Engheta, *Science* **2019**, *363*, 1333.
[50] A. Babaee, A. Momeni, A. Abdolali, R. Fleury, *Phys. Rev. Applied* **2021**, *15*, 044015.
[51] Z. Wang, G. Hu, X. Wang, X. Ding, K. Zhang, H. Li, S. N. Burokur, Q. Wu, J. Liu, J. Tan, C.-W. Qiu, *Nat. Commun.* **2022**, *13*, 2188.